



**HAL**  
open science

## Very high-resolution infrared imagery of misaligned tungsten monoblock edge heating in the WEST tokamak

A Grosjean, Y Corre, J Gaspar, J P Gunn, S Carpentier, X Courtois, R Dejarnac, E Delmas, G de Temmerman, M Diez, et al.

► **To cite this version:**

A Grosjean, Y Corre, J Gaspar, J P Gunn, S Carpentier, et al.. Very high-resolution infrared imagery of misaligned tungsten monoblock edge heating in the WEST tokamak. Nuclear Materials and Energy, 2021, 27, 10.1016/j.nme.2021.100910 . hal-03578420

**HAL Id: hal-03578420**

**<https://amu.hal.science/hal-03578420>**

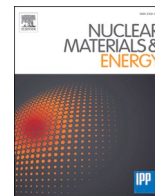
Submitted on 17 Feb 2022

**HAL** is a multi-disciplinary open access archive for the deposit and dissemination of scientific research documents, whether they are published or not. The documents may come from teaching and research institutions in France or abroad, or from public or private research centers.

L'archive ouverte pluridisciplinaire **HAL**, est destinée au dépôt et à la diffusion de documents scientifiques de niveau recherche, publiés ou non, émanant des établissements d'enseignement et de recherche français ou étrangers, des laboratoires publics ou privés.



Distributed under a Creative Commons Attribution - NonCommercial - NoDerivatives 4.0 International License



## Very high-resolution infrared imagery of misaligned tungsten monoblock edge heating in the WEST tokamak

A. Grosjean<sup>a,\*</sup>, Y. Corre<sup>a</sup>, J. Gaspar<sup>c</sup>, J.P. Gunn<sup>a</sup>, S. Carpentier<sup>d</sup>, X. Courtois<sup>a</sup>, R. Dejarnac<sup>b</sup>, E. Delmas<sup>a</sup>, G. De Temmerman<sup>d</sup>, M. Diez<sup>a</sup>, L. Dubus<sup>a</sup>, L. Dupont<sup>a</sup>, F. Escourbiac<sup>d</sup>, M. Firdaouss<sup>a</sup>, J. Gerardin<sup>b</sup>, M. Houry<sup>a</sup>, R. Pitts<sup>d</sup>, C. Pocheau<sup>a</sup>, E. Tsitrone<sup>a</sup>, the WEST team<sup>1</sup>

<sup>a</sup> CEA, Institute for Research on Fusion by Magnetic Confinement, 13108 Saint-Paul-Lez-Durance, France

<sup>c</sup> Aix Marseille Univ, CNRS, IUSTI, Marseille, France

<sup>d</sup> ITER Org, Route Vinon Sur Verdon, CS 90 046, F-13067 St Paul Les Durance, France

<sup>b</sup> Institute of Plasma Physics, Czech Academy of Sciences, 182 00 Prague, Czech Republic

### ARTICLE INFO

**Keywords:**  
Tungsten  
Monoblock  
WEST  
Infrared  
Heat flux  
Emissivity

### ABSTRACT

Fourteen ITER-like plasma-facing units (PFUs) made of bulk tungsten were installed in the WEST tokamak divertor. Five of which were misaligned with their poloidal leading edges (LEs) exposed to the plasma heat flux: two sharp-edge PFUs and three chamfered PFUs (vertical misalignment  $h = 0.30 \pm 0.1$  mm). The parallel heat flux is measured on the outer strike point with a very high-resolution (VHR) infrared camera, featuring a sub-millimeter spatial resolution ( $\sim 0.1$  mm/pixel). A Medium Wavelength IR filter (MWIR) was used to lower the temperature detection threshold ( $T_{\text{threshold, BB}} \approx 250$  °C) and extend the IR analysis to the full toroidal Monoblock (MB) length on both outer (OSP) and inner (ISP) strike points. The parallel heat flux derived from the VHR data ( $\sim 70$  MW/m<sup>2</sup>) is consistent with previous analysis and other measurements (Thermocouple and Fiber Bragg Grating) at the maximum heat flux location (OSP). This corresponds to real temperatures of about 1000 °C on the LE. Values obtained on the LE of the ISP are typically lower than of the OSP by a factor of two. However, a significant discrepancy between modeling and measurement is observed along with the toroidal temperature profile, with a temperature drop in the first 5 mm after the LEs. Visual and microscopic analysis performed on the component show clear evidence of surface state modification caused by plasma exposure: the presence of cracks on the LE, polished surface in its vicinity, and rougher surfaces further away from the LE.

### 1. Introduction

Next step divertors will face high, steady-state heat flux. A water-cooled divertor consisting of tungsten (W) monoblocks (MBs) bonded to CuCrZr cooling tubes is being manufactured for ITER to extract the high power coming from the plasma [1]. This technology is being tested in the WEST tokamak [2]. In WEST phase I, the magnetic field lines strike the nominal plasma-facing divertor surface at a glancing angle of  $\sim 3^\circ$  to spread the power. However, the subdivision of plasma-facing units (PFUs) into discrete MBs [1] with no specific shaping, means that the magnetic field lines can enter the gaps between them and strike their sides with near-normal incidence, leading to higher localized heat fluxes. This effect is enhanced by possible misalignments between MBs [3], which can lead to melting on the over-exposed LEs (see Fig. 1). The

WEST divertor is designed such that the plasma flowing along the magnetic field lines impacts the MB top surfaces at glancing angles (from  $0.5$  to  $2.5^\circ$  in the following experiments) [4]. The sinusoidal modulation of the incident angle with a  $20^\circ$  periodicity in the toroidal direction is caused by the so-called ripple effect induced by the 18 superconducting toroidal magnetic field coils installed in WEST (see background section of [5] for further details).

This paper is a continuation of the previous work on the thermal behavior of exposed LEs performed in the WEST test divertor sector during the C3 campaign (winter 2018) [5]. For the C4 experimental campaign (summer 2019) a new set-up was designed to simultaneously reduce the misalignments (toward WEST assembly tolerance:  $\pm 0.4$  mm) at the OSP and decrease the IR detection threshold to get extended temperature surface measurement on the whole MB as well as on the ISP

\* Corresponding author.

E-mail address: [agrosjea@utk.edu](mailto:agrosjea@utk.edu) (A. Grosjean).

<sup>1</sup> See <http://west.cea.fr/WESTteam>.

<https://doi.org/10.1016/j.nme.2021.100910>

Received 29 September 2020; Received in revised form 23 December 2020; Accepted 11 January 2021

Available online 17 January 2021

2352-1791/© 2021 The Authors.

Published by Elsevier Ltd.

This is an open access article under the CC BY-NC-ND license

(<http://creativecommons.org/licenses/by-nc-nd/4.0/>).

which is usually colder than the OSP. Repeated discharges with 4 MW injected RF power during a 6 s flat-top to reach a thermal equilibrium of the MBs and misalignment between neighboring PFUs inside the WEST assembly tolerance have been performed. The experimental configuration, the VHR system [6], and plasma conditions are depicted in Section 2. Compared to our previous studies, the upgrades performed on the VHR system lowered the temperature detection threshold ( $T_{\text{BB}} = 250\text{ }^{\circ}\text{C}$  instead of  $370\text{ }^{\circ}\text{C}$ ), which enables the IR analysis to be extended to the full toroidal MB length in the maximum heat flux area, which was not the case in [5], where it was limited to the few millimeters around the LE vicinity. In Section 3, the method developed in [5] is used to validate the toroidal symmetry of the parallel heat flux and estimate the power asymmetry between the inner and outer strike points. In this method, the heat flux, parallel to the magnetic field lines is assessed by matching the toroidal temperature profile on the LE with 3D finite element modeling, using a uniform heat load based on optical approximation (AO) with constant incident angle  $\alpha$ . The tungsten emissivity is assumed to be constant:  $\varepsilon = 0.4$ , which corresponds to that of damaged bulk tungsten in MWIR ( $\lambda = 3.9\text{ }\mu\text{m}$ ) [7]. Section 4 is dedicated to the discussion of singularities observed in the toroidal profile during the analysis. The toroidal heat flux distribution on the MB near the poloidal LE and its link to a possible inhomogeneity of the emissivity in the toroidal direction will be addressed. Embedded thermocouple (TC) and Fiber Bragg Grating (FBG) temperature measurements [8] performed on the W-coated graphite PFUs [9] are used to crosscheck the parallel heat flux derived from the IR camera. Postmortem emissivity measurements and complementary observations will be proposed to explain the discrepancy between modeled and infrared temperature.

## 2. Experimental configuration

The main limitation in the previous experiment [5] was the relatively high-temperature detection threshold which prevents measurement along with poloidal and toroidal profiles and was limited to 2–3 mm around the LE. To reduce this threshold, the wavelength of the filter was changed from small wavelength infrared (SWIR:  $1.6\text{ to }2.1\text{ }\mu\text{m}$ ) to medium wavelength infrared (MWIR:  $3.9 \pm 0.1\text{ }\mu\text{m}$ ). The temperature detection threshold was measured in the laboratory and found to be  $T_{\text{BB}} = 370\text{ }^{\circ}\text{C}$  and  $250\text{ }^{\circ}\text{C}$  with SWIR (C3 campaign) and MWIR (C4 campaign), respectively. The black body temperature detection threshold corresponds to the lower temperature detected by the VHR system, which means that the true temperature of the body ( $\varepsilon < 1$ ) has to be higher, to be detected (see the black line of Fig. 2). It has the advantage to significantly increase the area of the study and extend the

measurement to the ISP which is submitted to lower heat load than OSP because of power deposition asymmetry [10]. On the other hand, the emissivity variations due to different surface states are more pronounced in the MWIR filter: from 0.1 to 0.5 in MWIR while it was 0.3 to 0.6 in SWIR for pristine and damaged bulk tungsten, respectively [7]. The consequences of the black-body temperature can be seen in Fig. 2. The black-body temperature detection threshold is represented by the horizontal line ( $T_{\text{threshold, BB}} = 250\text{ }^{\circ}\text{C}$ ) while true temperature detection thresholds are plotted in vertical lines as a function of this emissivity:  $T_{\text{threshold, 0.4}} = 325 \pm 30\text{ }^{\circ}\text{C}$  (red) and  $T_{\text{threshold, 0.1}} = 500\text{ }^{\circ}\text{C}$  (blue). Fig. 2: Left: Planck's curves show the black body temperature as a function of the true temperature for a black body ( $\varepsilon = 1$  – dashed black), pristine bulk W ( $\varepsilon_w = 0.1$  – dashed blue), small cracks ( $\varepsilon_w = 0.3$  – blue), crack network ( $\varepsilon_w = 0.5$  – blue) and the mean emissivity was taken in the analysis ( $\varepsilon_w = 0.4$  – red) based on eq. (2) (see section 3.2 [5]).

Postmortem microscopy analysis performed on the overexposed LE after the C3 campaign reveals cracks network, on the exposed area, as well as on the first mm of the top surface of the MB (see right part of Fig. 2) [11]. Therefore, for the IR data analyses on the LE, the results presented in Section 3 are obtained with the assumption of a constant emissivity of 0.4, which corresponds to the average emissivity on the measurement performed on a surface with a crack network at  $500\text{ }^{\circ}\text{C}$  [7]. A constant emissivity is used to correct the black-body temperature on the toroidal profile (as performed in [5]). The parallel heat flux values given in Section 4 corresponds to the average values found for a 0.3 and 0.5 emissivity. Hence the error bars are covering the whole range of emissivity values from 0.3 to 0.5. In addition to the emissivity issues, the MWIR wavelength also degrades the spatial resolution of the system by a factor 2.3 corresponding to the ratio of the wavelength:  $3.9/1.7$  as it is limited by diffraction processes. Nonetheless, this degradation is compensated by the fact that the VHR is now equipped with software that optimizes the focus position for each Field of View (FoV). The modulation transfer function (MTF) of the instrument is modeled by a Gaussian in frequency space with a standard deviation ( $\sigma$ ), measured in the lab:  $0.175\text{ mm}$  for the C4 campaign instead of  $0.3\text{ mm}$  in C3. This means that the temperature discontinuities observed on the LE will be less impacted by the optical smoothing effect (developed in Figure 9 of [5]). To take these optical smoothing effects into account, a specific sensor correction was developed [6] and is applied based on the pixel size, the wavelength of the IR system, and the standard deviation of the MTF measured.

To investigate further the thermal behavior of exposed LEs and reduce the risk of melting during high power experiments, a new experimental configuration was designed for the C4 experimental

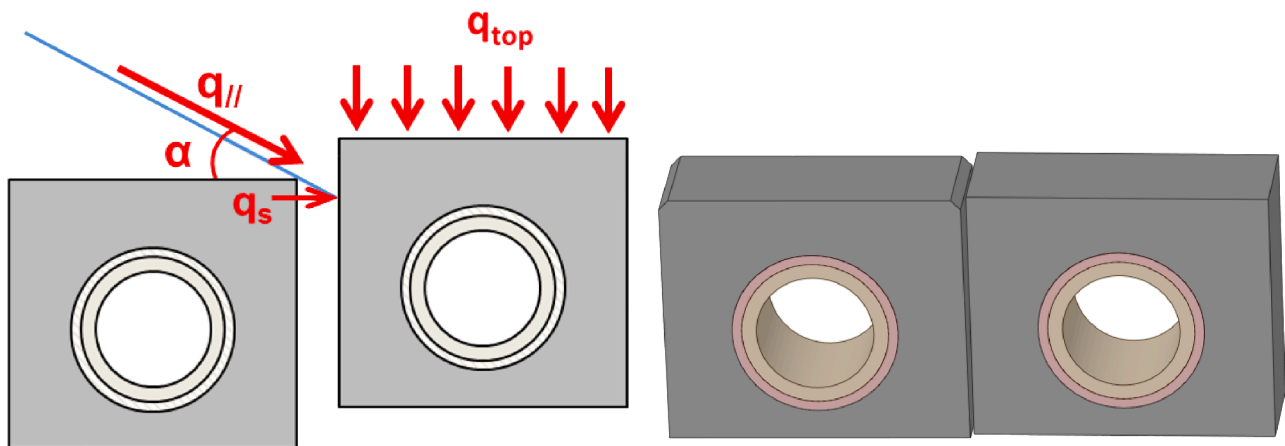


Fig. 1. Left – Magnetic field line impacting the side of the misaligned monoblock (blue line) with a parallel heat flux coming from the scrape-off layer ( $q_{//}$ ) and an incidence angle ( $\alpha$ ). Heat flux absorbed on the top surface ( $q_{\text{top}}$ ), and on the side surface ( $q_s$ ) are also depicted on the misaligned MB. Right – ITER-like PFU shaping used in WEST with chamfered edges:  $1\text{ mm} \times 1\text{ mm}$  on the left MB and sharp edges on the right MB. (For interpretation of the references to colour in this figure legend, the reader is referred to the web version of this article.)

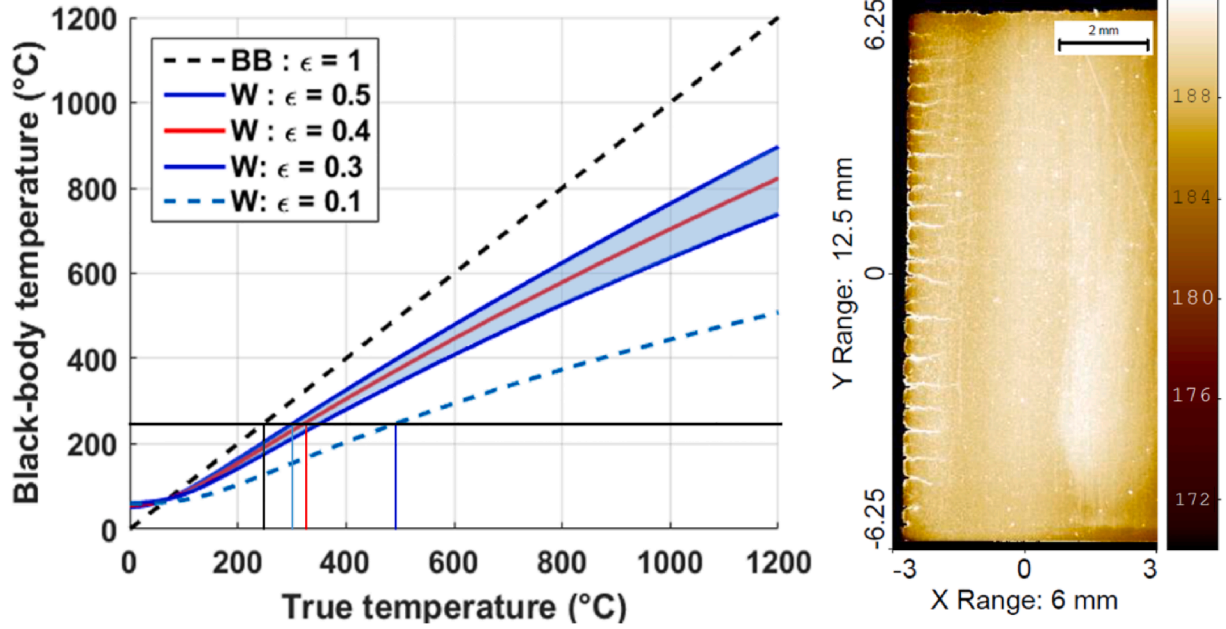


Fig. 2. Left: Planck's curves show the black body temperature as a function of the true temperature for a black body ( $\epsilon = 1$  – dashed black), pristine bulk W ( $\epsilon_w = 0.1$  – dashed blue), small cracks ( $\epsilon_w = 0.3$  – blue), crack network ( $\epsilon_w = 0.5$  – blue) and the mean emissivity was taken in the analysis ( $\epsilon_w = 0.4$  – red) based on eq. (2) (see section 3.2 [5]). Right: Confocal microscopy image (top view) of MB27 (sharp LE) on PFU #8 (former PFU #12) after the C4 experimental campaign. (For interpretation of the references to colour in this figure legend, the reader is referred to the web version of this article.)

campaign (2019) with reduced misalignments between PFUs (below or equal to the tolerance). Two new sharp ITER-like PFUs were installed in position #17 and #18 (see detailed shaping in the right side of Fig. 1). A metrological inspection was performed to monitor the vertical misalignments between neighboring PFUs required for the experiments with a 3D ball probe measuring arm before and after C4 and cross-checked with confocal microscopy in the regions of interest: two sharp (PFUs #8 and #17) and three having 1 mm chamfered edges (PFUs #7, #13, and #19). The results are listed in Table 1:

Based on the metrological inspection it is possible to identify eight regions of interest (ROIs) which have the greatest misalignments: PFUs #7-8, #13, #17, and #19 in both inner (ISP: MB15) and outer strike points (OSP: MB27). A dedicated experimental session has been performed with high stationary heat flux for at least 6 s to reach the thermal equilibrium of the MB. The same pulse is repeated each time with the FOV of the VHR focusing in a different ROI with main plasma parameters constant: injected power  $P_{inj} = 3.5 - 4.0$  MW, plasma current  $I_p = 500$  kA, and magnetic field  $B_T = 3.6$  T. Line-averaged density,  $\bar{n}_e$  is shown to vary slightly during the LH heating phase, in the range of  $3.6$  to  $3.9 \times 10^{19} \text{ m}^{-2}$  and reproducible from shot to shot (see Fig. 3).

Small discrepancies can be found regarding shots #54 936 and #54 969 with, respectively, 3.8 MW and 3.5 MW in terms of LH power, and 2.05 MW and 1.95 MW in terms of radiated power, instead of 4 MW and 2.2 MW for the other shots. Additionally, one shot (#54 969) experienced a reduction of power ( $-0.3$  MW for 200 ms) provoked by the real-time copper impurity safety interlock system (8.4 s). The power incident on the divertor  $P_{div}$  is computed as follows:

$$P_{div} = P_{inj} + P_{Ohm} - P_{rad} - P_{LH-losses} \quad (1)$$

$P_{inj}$  being the power injected with RF heating (MW),  $P_{Ohm}$  the ohmic power (MW),  $P_{rad}$  the radiated power (MW) measured by bolometry, and  $P_{LH-losses}$  the power deposited by vertically-drifting electrons trapped in the magnetic field ripple on the upper part of the machine, estimated with calorimetry.

### 3. Parallel heat flux estimation

In this section, the iterative method developed in [5] is applied to deduce the parallel heat flux that matches the experimental data from the LE to the trailing edge (toroidal profile), for a constant value of emissivity ( $\epsilon = 0.4$ ). The thermal modeling is performed on MB27 (30.6 mm toroidal length) assuming uniform heat flux on top and poloidal side surface calculated with the optical approximation as follows:

$$q_{top} = q_{||} \sin \alpha + q_{BG} \quad (2)$$

$$q_s = q_{||} \sin(\alpha + \beta) \quad (3)$$

where  $\alpha$  is the field line angle which is derived from the magnetic equilibrium and CAD model of the divertor (PFCFlux software [12]),  $\beta$  being the angle between the top and poloidal-side surface ( $90^\circ$  for a sharp edge and  $45^\circ$  for a 1x1 mm chamfer edge),  $q_{||}$  the heat flux density parallel to  $B$ ,  $q_{top}$ , and  $q_s$ , respectively, the heat flux densities absorbed on top and poloidal side surfaces. Here, the background heat flux ( $q_{BG}$ ),

Table 1

Metrological inspection results on misalignments between two neighboring PFUs. The misalignment is calculated as the height difference between the PFU and its neighbor facing the parallel heat flux i.e.  $h = z_n - z_{n-1}$  in the OSP and  $h = z_n - z_{n+1}$  in the ISP,  $n$  being the PFU number. The last row indicates the shape of the LE: chamfered (Ch) or sharp (Sh). Note that the misalignments are higher than assembly tolerances in the ISP, which is not critical in this case as a strong asymmetry in power deposition is expected between ISP and OSP [10].

PFU	# 7	# 8	# 9	# 10	# 11	# 12	# 13	# 14	# 15	# 16	# 17	# 18	# 19	# 20
h (mm) MB15	-0.30	<b>0.29</b>	-0.06	0.27	-0.24	0.01	<b>0.31</b>	0.06	0.04	-0.37	<b>0.67</b>	-0.37	<b>0.42</b>	0.17
h (mm) MB27	<b>0.28</b>	<b>0.40</b>	-0.27	-0.03	-0.18	0.18	<b>0.22</b>	-0.49	-0.41	0.02	<b>0.20</b>	-0.34	<b>0.15</b>	-0.52
Shape	Ch	Sh	Ch	Ch	Ch	Ch	Ch	Ch	Sh	Ch	Sh	Sh	Ch	Ch

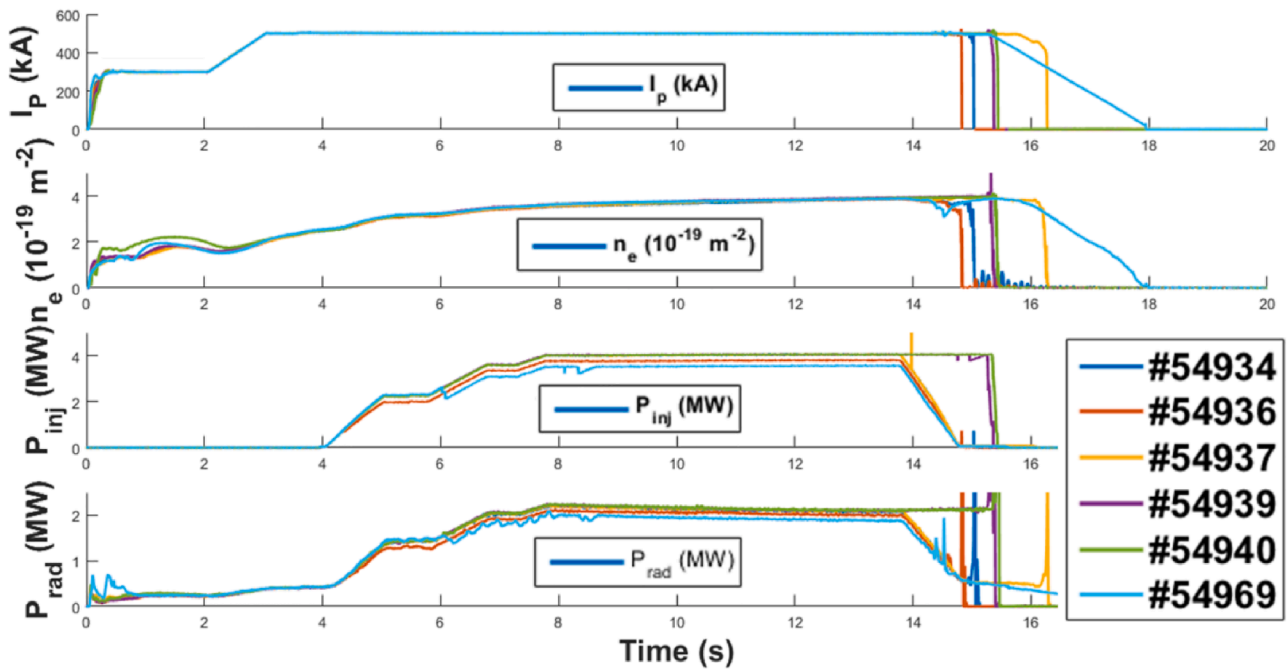


Fig. 3. Plasma characteristics of the shots studied in this paper: from top to bottom are shown plasma current (kA), line-averaged density ( $10^{19} \text{ m}^{-2}$ ), injected power (MW), and radiated power (MW). (For interpretation of the references to colour in this figure legend, the reader is referred to the web version of this article.)

including plasma radiation and neutral particles coming from charge exchange, is assumed to be homogeneous for simplicity and will be neglected in the rest of the study as the parallel heat flux is deduced for the LE. The wetted height of the LE ( $h_w$ ) which is directly exposed to the plasma heat flux depends on the misalignment of the component ( $h$ ), the gap between the two consecutive PFUs ( $g_{PFU}$ ), as well as the incidence angle at the strike point location for both sharp and chamfered geometries (see more details in [5]).

The analysis method shall be described in detail for shot #54 934, where the VHR IR data corresponds to PFUs #7 and #8 with the maximum heat flux located on MB27 (see left part of Fig. 4). Postmortem pictures were taken for every region of interest after the C4 campaign, the right part of Fig. 4 displays the FoV monitored by the VHR on shot #54 934. In this picture, one can notice the different surface states in the toroidal location which could explain, at least in part, the inhomogeneity of the emissivity.

Despite the high spatial resolution of the system (pixel size = 0.091

mm), optical blurring and deformation can be observed on very steep temperature gradients such as those on the sharp LEs.

A comparison between modeling and measurement is presented in Fig. 5 for PFUs #7 (top) and #8 (bottom) having 0.28 mm and 0.40 mm of vertical misalignment, respectively. The same method is applied to PFU #13, #17, and #19 and are summarized in Table 2.

PFU #7 and #8 are situated at the location of the maximum surface heat flux with respect to the toroidal ripple effect. The incidence angle of the magnetic field is  $2.3^\circ$ , the chamfered and sharp LE misalignment are, respectively, 0.28 mm and 0.40 mm. Similarly to the previous analysis, the parallel heat flux is adjusted to match the temperature data near the LE (up to 1 mm and 3 mm away from the sharp and chamfered LE, respectively) assuming a constant emissivity ( $\epsilon = 0.4$ ). The best match between synthetic and experimental IR data is obtained with  $q_{\parallel} = 78.5 \pm 9 \text{ MW.m}^{-2}$  and  $q_{\parallel} = 65 \pm 7 \text{ MW.m}^{-2}$  for the chamfered and the sharp LE, respectively, which is consistent with the value of  $q_{\parallel} = 67 \pm 6 \text{ MW.m}^{-2}$  computed with FBG measurement in W-coated graphite

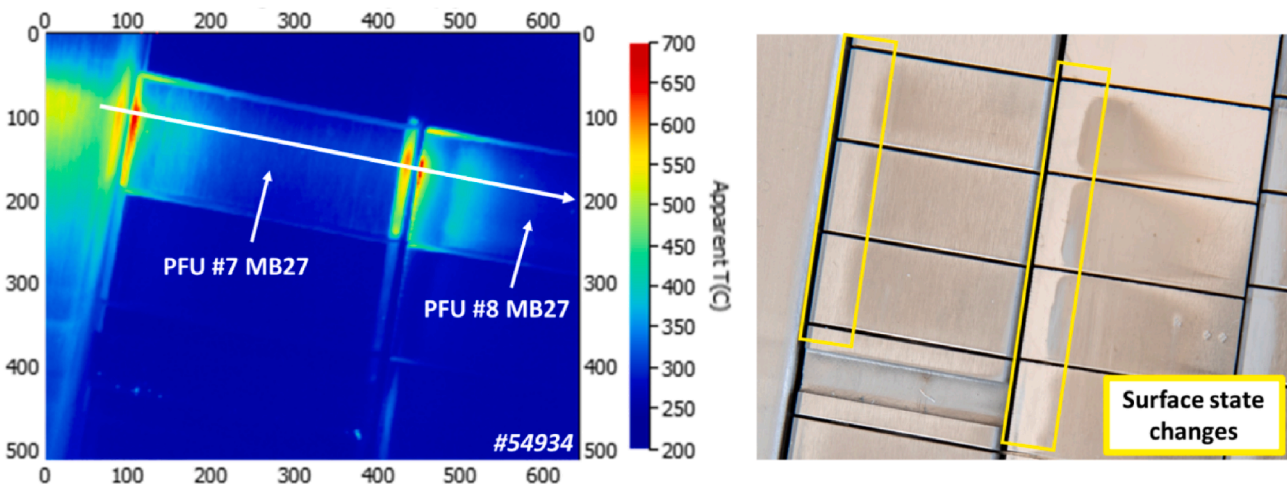


Fig. 4. Shot #54 934 on PFU #7 (chamfered edge –  $h = 0.28 \text{ mm}$ ) and PFU #8: (sharp edge –  $h = 0.40 \text{ mm}$ ). Left: IR data frame (13.78 s) with MWIR filter ( $3.9 \mu\text{m}$ ), which exhibits local heating on MB27. Right: Picture of the FoV showing the different surface states.

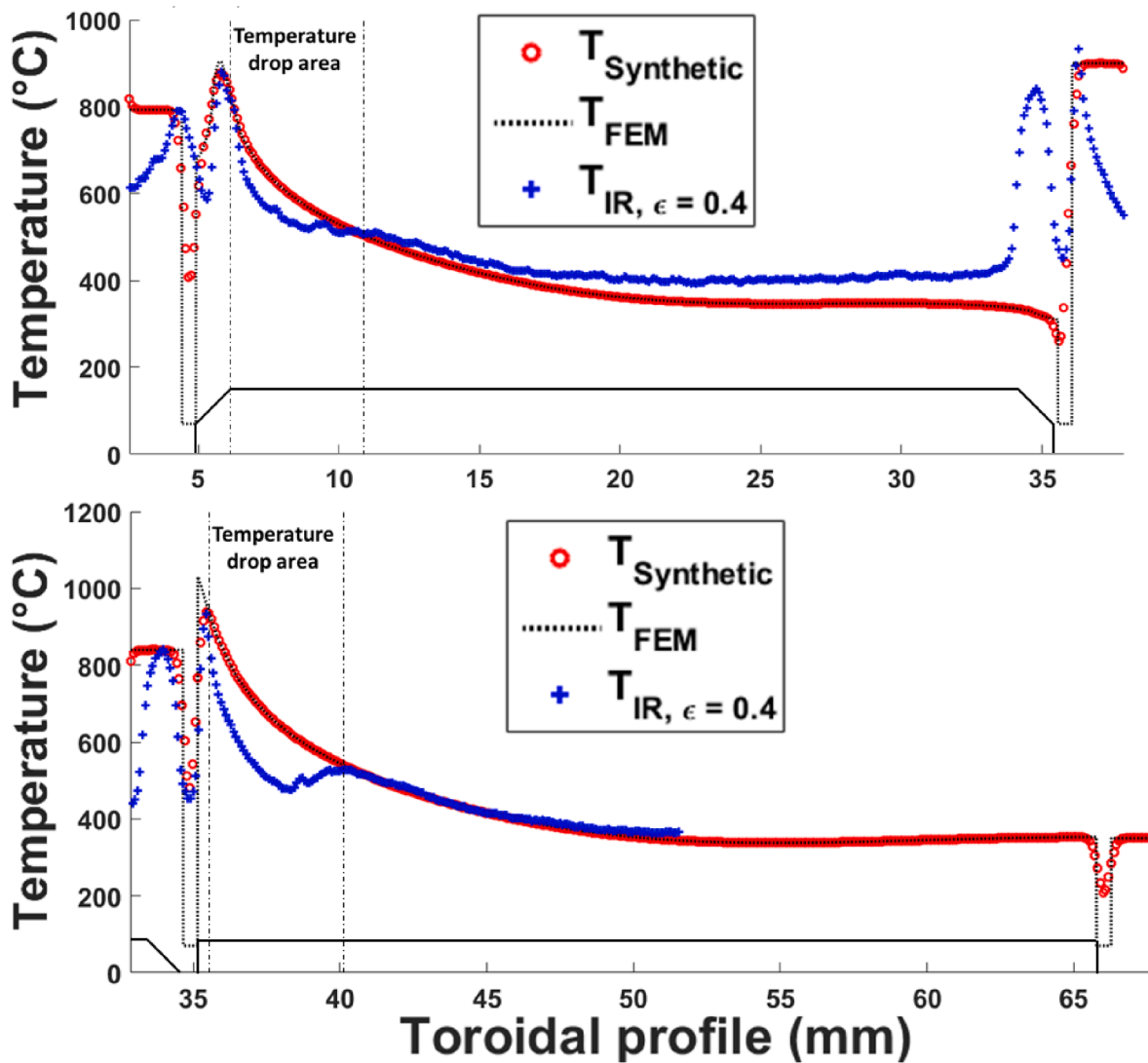


Fig. 5. Comparison between experimental IR (blue corrected with  $\epsilon_w = 0.4$ ) and synthetic temperature (red) based on thermal modeling (dark) on the full toroidal profile of PFUs #7 (top) and #8 (bottom). The temperature drop area was highlighted for both geometries and can be visually observed in Fig. 4. (For interpretation of the references to colour in this figure legend, the reader is referred to the web version of this article.)

Table 2

Summary of the LE experiment performed during the C4 experimental campaign with the MWIR filter. The table shows the shot number, the PFU number, the shaping, the misalignment (h), averaged incident angle ( $\alpha$ ) in the toroidal direction, the averaged  $P_{div}$  in the plateau (6.8 to 13.8 s), the maximum black body temperature ( $T_{IR}$ ) observed at the LE, the parallel heat flux calculated ( $q_{//, VHR}$ ), the parallel heat flux calculated with FBG ( $q_{//, FBG}$ ) are reported in the table.

Shot	PFU/MB	Shaping	h (mm)	$\alpha$ (°)	$P_{div}$ (MW)	$T_{IR}$ (°C)	$q_{//, VHR}$ (MW.m <sup>-2</sup> )	$q_{//, FBG}$ (MW.m <sup>-2</sup> )
54 934	7/27	Ch	0.28	$2.3 \pm 0.1$	1.804	645	$78.5 \pm 9$	$67.1 \pm 6$
54 934	8/27	Sh	0.40	$2.2 \pm 0.1$	1.804	675	$65 \pm 7$	$67.1 \pm 6$
54 936	13/27	Ch	0.22	$1.4 \pm 0.1$	1.667	475	$89 \pm 9$	$61.1 \pm 5$
54 937	17/27	Sh	0.20	$0.6 \pm 0.1$	1.801	360	$89.5 \pm 11$	$66.7 \pm 6$
54 939	19/27	Ch	0.15	$0.4 \pm 0.1$	1.797	310	$92 \pm 12$	$65.1 \pm 6$
54 940	17/15	Sh	0.67	$1.1 \pm 0.1$	1.787	430	$35.5 \pm 3$	$23.3 \pm 2$
54 969	13/15	Ch	0.31	$1.7 \pm 0.1$	1.558	245	$38.5 \pm 5$	$21.8 \pm 2$

components (#54 934). As a reminder, FBG is embedded thermal sensors with a 12.5 mm spatial resolution in the poloidal direction implemented with 3.5 mm and 7.0 mm depths [8]. FBGs are immune to electromagnetic interference and independent of W surface emissivity. Surface heat flux calculations ( $q_{top}$ ) were performed for each pulse based on the embedded temperature measured by FBG as described in [13]. Since the FBG process provides the heat flux absorbed on the top surface ( $q_{top}$ ), the incidence angle is required to obtain the parallel heat flux

using Eq. (2). FBG estimations are performed in inertial W-coated graphite PFUs located in the maximum heat flux area (equivalent to PFU #7 as shown in Fig. 2), where the angle is  $3.4 \pm 0.15^\circ$ .

#### 4. Discussion

The experimental temperature profiles show a significant temperature drop from 0.3 mm to 5 mm after the LE on PFUs #7 and #8. In this

area, an almost 200 °C difference between the simulation and experimental data is reported. This is attributed to the surface emissivity effect that could be reduced down to 0.2 locally, introducing an artificial temperature drop as measured with the IR system, using constant emissivity, and observed in postmortem pictures (see Fig. 4). A similar effect has also been observed in PFU #13 while it is not possible to observe on PFUs #17 and #19 because the surface temperature is below the VHR detection threshold. This is consistent with the simulation that predicts surface temperatures lower than 350 °C in the polished area (from 0.3 to 5 mm), which corresponds to 220 °C black-body temperature assuming an emissivity  $\epsilon = 0.2$ ; and thus lower than the temperature detection threshold ( $T_{\text{threshold, BB}} = 250$  °C). The IR scene in PFUs #7–8 is complex and arises due to many physical and technical phenomena which are hard to discretize. Further analysis is being processed on surface state emissivity, erosion-redeposition quantification, and impurity content to help understanding better the singularities observed on the toroidal profiles.

Further away on the top surface of the MB (from 5 mm to 15 mm), simulation and IR data are in better agreement, especially on PFU #8, suggesting that the constant emissivity of 0.4 is consistent with the top surface of the ITER-like MB at the OSP. In this region, visual inspection (see Fig. 4) shows clear evidence of roughening. The PFU #7 shows a similar trend on the left side of the MB and a slightly different trend further away (on the right side of the MB), with a higher IR temperature ( $\sim 30^\circ$  higher) than the FEM temperature (a region which is not affected anymore by the LE). This can be explained by a higher emissivity, which would be feasible as the materials and manufacturing process are different between PFU #7 and #8, which may affect the surface state of pristine tungsten. The other reason that may be given is that the hot sharp PFU #8 LE is radiating on the top surface of PFU #7 and additional photons are collected by the VHR leading to an overestimate of the top black-body temperature surface. Postmortem emissivity measurements are foreseen in the laboratory to elucidate this issue.

Similar analysis was also performed on PFU #13, #17, and #19 further away in the ripple modulation, featuring lower and higher heat load on the top surface area on the low field side (OSP) and high field side (ISP) areas, respectively. The results are summarized in the Table 2.

The analyses at the ISP, despite low temperature, give interesting results for sharp (PFU #17 shot #54 940) and chamfered edge (PFU #13 shot #54 969) with, respectively,  $35.5 \pm 3$  MW.m<sup>-2</sup> and  $38.5 \pm 5$  MW.m<sup>-2</sup> parallel heat flux. Given the conditions: low temperature and lack of information on the emissivity, both results are consistent together and the estimation may be over evaluated as the emissivity at the ISP is expected to be higher, due to redeposition areas observed in the right panel of Fig. 6. FBG reports  $23.3 \pm 2$  and  $21.8 \pm 2$  MW.m<sup>-2</sup>,

respectively, with lower values as expected, and lower dispersion. This higher uncertainty is attributed to emissivity uncertainty in MWIR (see Fig. 6) that has to be reduced with postmortem emissivity.

The parallel heat flux reported on the ISP ( $37$  MW.m<sup>-2</sup>) is about half of the value found on the OSP ( $83$  MW.m<sup>-2</sup>). The result is independent of the MB geometry, sharp or chamfered LEs (PFU #17 and #13, respectively). For this set of experiments, a strong divertor asymmetry is observed in favor of the outer side as expected with particle drift theory in the forward magnetic field [10]. On the OSP, the heat load is more important, between  $65$  MW.m<sup>-2</sup> and  $92$  MW.m<sup>-2</sup>. The IR measurements agree well with the FBG measurements (from  $65$  MW.m<sup>-2</sup> to  $67$  MW.m<sup>-2</sup>) for PFUs #7 and #8 (high heat flux on the top surface due to the ripple effect) but give higher values for PFUs #13, #17, and #19 (low heat flux on the top surface).

The parallel heat flux should be constant [5]. There are several reasons to explain this discrepancy. First, the surface emissivity can strongly vary from one LE to another one and be significantly higher ( $>0.5$ ) in the low heat flux area (grazing angle). Second, the temperature reported on the LE is lower at the grazing incident angle (typically  $\leq 700$  °C near the LE) and may not be as reliable as it can be for other PFUs ( $\sim 1000$  °C). The signal can be polluted by multiple reflections occurring in the vacuum vessel, which is hard to quantify. The uncertainty measurements on the lower temperature are under investigation, the uncertainty tends to be higher for low temperatures, close to the detection threshold. The third reason comes from the accuracy of the misalignment's measurement. At this location, the misalignments are lower ( $\leq 0.2$  mm) and therefore, the calculation becomes more sensitive to the accuracy as shown in the error bars reported in Table 2, including  $\pm 20$   $\mu$ m uncertainties on the exposed height of the LE. The last reason can be due to the gyro-radius effect which becomes more important when [14,15]. To be able to conclude, postmortem emissivity measurements are required to evaluate the uncertainty implied by the emissivity before investigating the other possibilities.

In a more general aspect, one can see that estimated heat fluxes are higher in chamfered geometries than for sharp edges that can be attributed to higher emissivity on the chamfer or an overcorrection of MTF characterizing the smoothing effect on the sharp edge [16]. This assumption will be verified as soon as the PFU is available for post-mortem emissivity measurement.

The parallel heat flux values measured on shot #54 934 with high temperature and relatively high misalignment of  $78.5 \pm 9$  MW.m<sup>-2</sup> and  $65 \pm 7$  MW.m<sup>-2</sup> are considered more reliable because the temperature is higher and results are closer to the FBG estimations.

In this context, there is a major interest in reducing the uncertainty of the emissivity to a specific time study and go deeper in the heat load

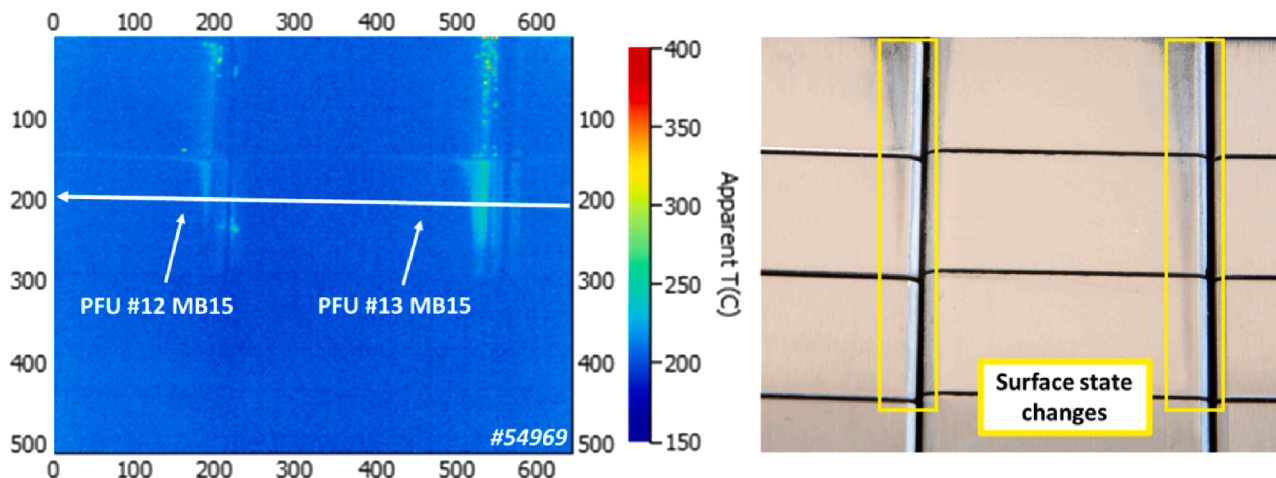


Fig. 6. Shot #54 969 on PFU #13 (chamfered edge –  $h = 0.31$  mm). Left: IR data frame (13.78 s) with MWIR filter ( $3.9$   $\mu$ m), which exhibits local heating on MB15. Right: Picture of the FoV showing the different surface states.

physics analysis without uncertainty issues. In the near future, the possibility to measure the emissivity of the actively cooled ITER-like PFUs inside the tokamak, based on the double heating method developed in [17] has to be investigated to improve the thermography measurement accuracy.

## 5. Conclusion

New experiments have been successfully achieved in the C4 experimental campaign (2019) with reduced PFU misalignments and optimized IR settings (MWIR filter) to reduce the detection threshold. Parallel heat flux was measured on deliberately misaligned poloidal LEs assuming constant emissivity ( $\varepsilon = 0.4 \pm 0.1$ ) to take into account the cracks that are observed near the LE. Resulting parallel heat fluxes show good consistency for two PFU located in the maximum heat flux area (PFU #7 – Chamfered and #8 – sharp), which confirms the results obtained in C3 campaign that was obtained with limited area [2] (only few mm near the LE), higher misalignment (up to 0.8 mm) and lower parallel heat flux ( $45 \text{ MW.m}^{-2}$  and  $70 \text{ MW.m}^{-2}$  in the former and new experiment respectively). A quantitative agreement is found with the FBG temperature probes proving the overall consistency between two independent measurements applied to different components (standard inertial W-coated PFUs and ITER-like actively cooled PFUs). The upgrades on the VHR has highlighted a net temperature drop in the vicinity of the LE (in the first 5 mm where steep temperature gradients are measured) inconsistent with thermal modelling. This can be correlated to emissivity drop as suggested by pictures taken after the C4 campaign exhibiting what seems to be polished surfaces. Further away, for the rest of the toroidal profile exhibiting rougher surface, up to the region which is not impacted by the LE, the experimental data are in good agreement with simulation having 0.4 emissivity.

However, slight differences was observed on the parallel heat flux ( $\sim 20 \text{ MW.m}^{-2}$ ) in other PFUs measured in this study while it is expected to be constant toroidally. This can be also correlated to emissivity variation from maximum to minimum heat flux areas.

The optimization of the VHR system enabled to get the first measurements on the LE PFUs located at the ISP. The outer and inner heat flux ratio is found to be clearly asymmetric for both VHR (70 – 30 %) and FBG measurements (75 – 25%), as expected with the drift flows in forward magnetic field [10].

Postmortem emissivity measurements are scheduled in the upcoming months to confirm the interpretation given in the paper. Also, further analysis is planned such as confocal microscopy to observe the surface microstructure in this specific area and see whether this emissivity drop is caused by cracks, sputtering, or redeposition from the exposed poloidal edge.

## Declaration of Competing Interest

The authors declare that they have no known competing financial interests or personal relationships that could have appeared to influence the work reported in this paper.

## Acknowledgement

Work performed under EUROfusion WP PFC. This work has been carried out within the framework of the EUROfusion Consortium and has received funding from the Euratom research and training programme 2014-2018 and 2019-2020 under grant agreement No 633053. The views and opinions expressed herein do not necessarily reflect those of the European Commission.

## References

- [1] M. Missirlian, M. Firdaouss, M. Richou, P. Languille, S. Lecocq, M. Lipa, The WEST project: PFC shaping solutions investigated for the ITER-like W divertor, *Fusion Eng. Des.* 88 (9) (Oct. 2013) 1793–1797, <https://doi.org/10.1016/j.fusengdes.2013.03.048>.
- [2] J. Bucalossi, M. Missirlian, P. Moreau, F. Samaille, E. Tsitrone, D. van Houtte, T. Batal, C. Bourdelle, M. Chantant, Y. Corre, X. Courtois, L. Delpech, L. Doceul, D. Douai, H. Dougnac, F. Faisse, C. Fenzi, F. Ferlay, M. Firdaouss, L. Gargiulo, P. Garin, C. Gil, A. Grosman, D. Guilhem, J. Gunn, C. Hernandez, D. Keller, S. Larroque, F. Leroux, M. Lipa, P. Lotte, A. Martinez, O. Meyer, F. Micolon, P. Mollard, E. Nardon, R. Nouaillietas, A. Pilia, M. Richou, S. Salasca, J.-M. Travère, The WEST project: Testing ITER divertor high heat flux component technology in a steady state tokamak environment, *Fusion Eng. Des.* 89 (7–8) (2014) 907–912, <https://doi.org/10.1016/j.fusengdes.2014.01.062>.
- [3] J.P. Gunn, S. Carpentier-Chouchana, F. Escourbiac, T. Hirai, S. Panayotis, R. A. Pitts, Y. Corre, R. Dejarnac, M. Firdaouss, M. Kočan, M. Komm, A. Kukushkin, P. Languille, M. Missirlian, W. Zhao, G. Zhong, Surface heat loads on the ITER divertor vertical targets, *Nucl. Fusion* 57 (4) (2017) 046025, <https://doi.org/10.1088/1741-4326/aa5e2a>.
- [4] M. Missirlian, J. Bucalossi, Y. Corre, F. Ferlay, M. Firdaouss, P. Garin, A. Grosman, D. Guilhem, J. Gunn, P. Languille, M. Lipa, M. Richou, E. Tsitrone, The WEST project: current status of the ITER-like tungsten divertor, *Fusion Eng. Des.* 89 (7–8) (2014) 1048–1053, <https://doi.org/10.1016/j.fusengdes.2014.01.050>.
- [5] A. Grosjean, Y. Corre, R. Dejarnac, J. Gaspar, J.P. Gunn, S. Carpentier-Chouchana, X. Courtois, E. Delmas, G. De Temmerman, M. Diez, L. Dubus, A. Durocher, F. Escourbiac, M. Firdaouss, J. Gerardin, M. Houry, R.A. Pitts, C. Pocheau, E. Tsitrone, First analysis of the misaligned leading edges of ITER-like plasma facing units using a very high resolution infrared camera in WEST, *Nucl. Fusion* 60 (10) (2020) 106020, <https://doi.org/10.1088/1741-4326/ab9fa6>.
- [6] M. Houry, C. Pocheau, M.-H. Aumeunier, C. Balorin, K. Blanckaert, Y. Corre, X. Courtois, F. Ferlay, J. Gaspar, S. Gazzotti, A. Grosjean, T.H. Loarer, H. Roche, A. Saille, S. Vives, The very high spatial resolution infrared thermography on ITER-like tungsten monoblocks in WEST Tokamak, *Fusion Eng. Des.* 146 (2019) 1104–1107, <https://doi.org/10.1016/j.fusengdes.2019.02.017>.
- [7] J. Gaspar, C. Pocheau, Y. Corre, N. Ehret, D. Guilhem, M. Houry, T. Loarer, T. h. Loewenhoff, C. Martin, C. Pardanau, G. Pintsuk, M. Richou, F. Rigollet, H. Roche, G. Sepulcre, M. Wirtz, Emissivity measurement of tungsten plasma facing components of the WEST tokamak, *Fusion Eng. Des.* 149 (2019) 111328, <https://doi.org/10.1016/j.fusengdes.2019.111328>.
- [8] Y. Corre, G. Laffont, C. Pocheau, R. Cotillard, J. Gaspar, N. Roussel, M. Firdaouss, J.-L. Gardarein, D. Guilhem, M. Missirlian, Integration of fiber Bragg grating temperature sensors in plasma facing components of the WEST tokamak, *Rev. Sci. Instrum.* 89 (6) (2018) 063508, <https://doi.org/10.1063/1.5024514>.
- [9] M. Firdaouss, Y. Corre, P. Languille, H. Greuner, E. Autissier, C. Desgranges, D. Guilhem, J.P. Gunn, M. Lipa, M. Missirlian, J.-Y. Pascal, C. Pocheau, M. Richou, E. Tsitrone, Operational limits on WEST inertial divertor sector during the early phase experiment, *Phys. Scr.* T167 (2016) 014012, <https://doi.org/10.1088/0031-8949/2016/T167/014012>.
- [10] R.A. Pitts, P. Andrew, X. Bonnin, A.V. Chanikin, Y. Corre, G. Corrigan, D. Coster, I. Duran, T. Eich, S.K. Erements, W. Fundamenski, A. Huber, S. Jachmich, G. Kirnev, M. Lehnen, P.J. Lomas, A. Loarte, G.F. Matthews, J. Rapp, C. Silva, M.F. Stamp, J. D. Strachan, E. Tsitrone, Edge and divertor physics with reversed toroidal field in JET, *J. Nucl. Mater.* 337–339 (2005) 146–153, <https://doi.org/10.1016/j.jnucmat.2004.10.111>.
- [11] M. Diez, J.P. Gunn, M. Firdaouss, A. Grosjean, Y. Corre, E. Delmas, L. Gargiulo, E. Tsitrone, First evidence of optical hot spots on ITER-like plasma facing units in the WEST tokamak, *Nucl. Fusion* 60 (5) (2020) 054001, <https://doi.org/10.1088/1741-4326/ab7891>.
- [12] M. Firdaouss, T. Batal, J. Bucalossi, P. Languille, E. Nardon, M. Richou, Heat flux depositions on the WEST divertor and first wall components, *Fusion Eng. Des.* 98–99 (2015) 1294–1298, <https://doi.org/10.1016/j.fusengdes.2014.12.024>.
- [13] J. Gaspar, Y. Corre, M. Firdaouss, J.L. Gardarein, J. Gerardin, J.P. Gunn, M. Houry, T. Loarer, T. Loarer, M. Missirlian, J. Morales, P. Moreau, C. Pocheau, E. Tsitrone, First heat flux estimation in the lower divertor of WEST with embedded thermal measurements, *Fusion Eng. Des.* 146 (2019) 757–760, <https://doi.org/10.1016/j.fusengdes.2019.01.074>.
- [14] J.P. Gunn, S. Carpentier-Chouchana, R. Dejarnac, F. Escourbiac, T. Hirai, M. Komm, A. Kukushkin, S. Panayotis, R.A. Pitts, Ion orbit modelling of ELM heat loads on ITER divertor vertical targets, *Nucl. Mater. Energy* 12 (2017) 75–83, <https://doi.org/10.1016/j.nme.2016.10.005>.
- [15] R. Dejarnac, M. Komm, J.P. Gunn, Z. Pekarek, Effect of misaligned edges and magnetic field orientation on plasma deposition into gaps during ELMs on ITER, *J. Nucl. Mater.* 415 (1(Supplement)) (2011) S977–S980, <https://doi.org/10.1016/j.jnucmat.2010.09.042>.
- [16] M.-H. Aumeunier, et al., Infrared thermography in metallic environments of WEST and ASDEX Upgrade, *Nucl. Mater. Energy* 26 (Mar. 2021) 100879, <https://doi.org/10.1016/j.nme.2020.100879>.
- [17] J. Gaspar, et al., In-situ assessment of the emissivity of tungsten plasma facing components of the WEST tokamak, *Nucl. Mater. Energy* 25 (Dec. 2020) 100851, <https://doi.org/10.1016/j.nme.2020.100851>.